Structure and kinematics of edge-on galaxy discs - III. The rotation curves in the gas

Kregel, M.; van der Kruit, P. C.

Published in:
Monthly Notices of the Royal Astronomical Society

DOI:
10.1111/j.1365-2966.2004.07978.x

Publication date:
2004

Mon. Not. R. Astron. Soc. **352,** 787–803 (2004) doi:10.1111/j.1365-2966.2004.07978.x

Structure and kinematics of edge-on galaxy discs – III. The rotation curves in the gas

M. Kregel[1] and P. C. van der Kruit[1⋆]

[1] *Kapteyn Astronomical Institute, University of Groningen, PO Box 800, 9700AV Groningen, the Netherlands*

Accepted 2004 April 28. Received 2004 April 28; in original form 2004 March 16

ABSTRACT

A technique is introduced for deriving the gaseous rotation curves of edge-on spiral galaxies. The entire major axis position–velocity (XV) diagram is modelled with a set of rings in a least-squares sense, allowing for the effects of beam-smearing and line-of-sight projection. The feasibility of the technique is demonstrated by applying it to good quality H I XV diagrams of eight edge-on spirals. For seven additional spirals the XV diagrams are of insufficient quality, and the H I rotational velocities derived earlier using the envelope-tracing method are retained. The H I results are augmented with the optical emission line (H II) kinematics to arrive at estimates of the full rotation curves. A detailed comparison of the H I and H II kinematics shows that the discs in our sample are sufficiently transparent at the heights above the plane where we have taken our optical spectra to derive the stellar kinematics. In several of these spirals the H II is mainly confined to the spiral arms and does not extend out to the edge of the H I layer, which may have caused the H II velocity profiles to be significantly narrower than those of H I.

Key words: galaxies: fundamental parameters – galaxies: kinematics and dynamics – galaxies: spiral – galaxies: structure.

1 INTRODUCTION

The large-scale circular motion of the interstellar gas in spiral galaxies balances the radial gradient of the gravitational potential. The readiness with which this circular motion can be derived from spectroscopic observations of gaseous emission lines such as H I, CO and Hα has prompted numerous studies aimed at reconstructing the radial mass distribution (e.g. Kent 1986; Begeman 1987; Verheijen 1997; Palunas & Williams 2000; de Blok et al. 2001; Sofue et al. 2003; Swaters et al. 2003). These studies focus on galaxies of intermediate inclination, because a given line of sight or beam then yields a simple velocity profile, which originates at a single galactocentric radius. In this case the velocity field, i.e. the first moment of each of the velocity profiles, can be taken as representative for the true circular velocity. For a line of sight towards an edge-on spiral, however, a velocity profile consists of a superposition of gas clouds from a large range of galactocentric radii, each having a different line-of-sight velocity. Thus, for spirals seen edge-on a first moment analysis is clearly inadequate. Nevertheless, edge-on spirals offer a unique perspective for studying a host of properties related to the vertical structure of spiral galaxies. Examples include the vertical light and colour profiles of stellar discs (van der Kruit & Searle 1981a,b 1982; de Grijs, Peletier & van der Kruit 1997; Kuchinski et al. 1998), the kinematics and vertical structure of bulges and bars (Kuijken & Merrifield 1995; Aronica et al. 2003), the nature of stellar haloes and thick discs (Sackett et al. 1994; Dalcanton & Bernstein 2002), the gaseous disc–halo interface (Swaters, Sancisi & van der Hulst 1997; Collins et al. 2000) and the distribution of interstellar dust (Howk & Savage 1999; Alton et al. 2000). To study any of these properties in relation to the global dynamics or mass composition requires the ability to derive the rotation curves of edge-on spirals.

This is the third paper in a series[1] in which we aim to provide new constraints on the dynamics of spiral galaxy discs through an observational synthesis of the global stellar disc structure and kinematics. The series is preceded by a re-analysis (Kregel, van der Kruit & de Grijs 2002, hereafter referred to as KKG) of the surface photometry in the *I*-band of the sample of edge-on galaxies from de Grijs (1997, 1998). In Paper I in the series (Kregel, van der Kruit & Freeman 2004a) we presented optical spectroscopy to study the stellar kinematics in 17 edge-on galaxies taken from this sample. In Paper II (Kregel, van der Kruit & de Blok 2004b) we presented H I synthesis observations of 15 of these galaxies and derived rotation curves using the envelope-tracing method. In this paper we will introduce an automated method to derive rotation curves by fitting the

⋆E-mail: vdkruit@astro.rug.nl

[1] The series contains adapted versions of most chapters in the PhD thesis of MK (Kregel 2003).

full position–velocity (XV) diagram and apply that to eight of these galaxies with sufficient signal-to-noise (S/N) ratio. In addition to the circular velocity curves from the H I observations here we will further analyse the optical emission line spectroscopy (Paper I). In Paper IV (Kregel & van der Kruit 2004) we will analyse the stellar kinematics data of Paper I and correct for the line-of-sight effects using the circular velocity curves and finally present a general discussion in Paper V (Kregel, van der Kruit & Freeman 2004c).

For edge-on spirals an envelope-tracing (terminal velocity) method is often used to obtain the rotation curve from an H I or CO major axis position–velocity diagram (Sancisi & Allen 1979; Sofue 1996; García-Ruiz, Sancisi & Kuijken 2002). The main drawbacks of envelope-tracing methods are that they do not properly include the effects of beam smearing and the line-of-sight projection and use a small fraction of the data. An attractive alternative method is to simulate the entire XV diagram by manually adjusting the rotation curve and surface density profile until a visual match with the observed XV diagram is achieved (van der Kruit 1981; Rand 1994). The construction of a model XV diagram allows one to include and hence correct for the effects of beam smearing and line-of-sight projection. In addition, the rotation curve is determined using the entire XV diagram. Moreover, the XV diagram of the residuals, left after subtracting the model from the observed XV diagram, provides information concerning the presence of gas at small galactocentric radii and possible deviations from axisymmetry and/or non-circular motion. The obvious disadvantage of the method as applied previously, however, was its subjectivity.

The iteration procedure for deriving rotation curves in edge-on galaxies from H I observations by simulating the XV diagram was automated and enhanced by incorporating a least-squares fitting routine. This technique is described in Section 2, which also includes Monte Carlo tests on artificial XV diagrams. Its application to the observed H I XV diagrams of eight edge-on spirals is detailed in Section 3. Then, to complement the H I rotation curves at small radii, the kinematics of the optical emission lines, obtained as part of the spectroscopy presented in Paper I are analysed. A synthesis of the H II kinematics and the H I rotation curves is presented in Section 4. The H I and H II kinematics and the estimated full rotation curves are discussed in Section 5, giving specific attention to the effect of dust extinction. The most important findings are summarized in Section 6.

2 THE ROTATION CURVES OF EDGE-ON GALAXIES

2.1 The envelope-tracing method

In edge-on spirals, which are often unresolved along their minor axis, a single beam samples the gas density and kinematics across a large range in galactocentric radius. All the available information concerning the gas density and kinematics then condenses in the XV diagram. To illustrate this, the H I XV diagram expected for an edge-on view of the intermediately inclined Sbc galaxy NGC 2403 was simulated, using the H I density profile and rotation curve determined by Fraternali et al. (2002). NGC 2403 is suitable for this exercise because it is well-resolved and its main H I layer is symmetric and essentially in pure circular rotation (but see Fraternali et al. 2002, for the detection of a faint kinematically anomalous component). The velocity profiles were calculated assuming axisymmetry, transparency, pure circular rotation and a constant isotropic velocity dispersion $\sigma_{\rm gas}$ of 10 km s^{-1}

$$f(R', v) = \frac{1}{\sqrt{2\pi}\sigma_{\rm gas}} \int {\rm d}s\, \Sigma_{\rm gas}(R). \times \exp\left\{-\frac{[v - v_c(R)(R'/R)]^2}{2\,\sigma_{\rm gas}^2}\right\}, \quad (1)$$

$$R = \sqrt{R'^2 + s^2},$$

where R' is the radius projected on the sky, s is the line-of-sight coordinate ($s = 0$ at the line of nodes), R is the galactocentric radius, $\Sigma_{\rm gas}(R)$ is the face-on surface density profile and $v_c(R)$ the rotation curve. The result is illustrated in Fig. 1.

Under the assumptions of axisymmetry, transparency and circular rotation the extreme-velocity envelope of the XV diagram traces the

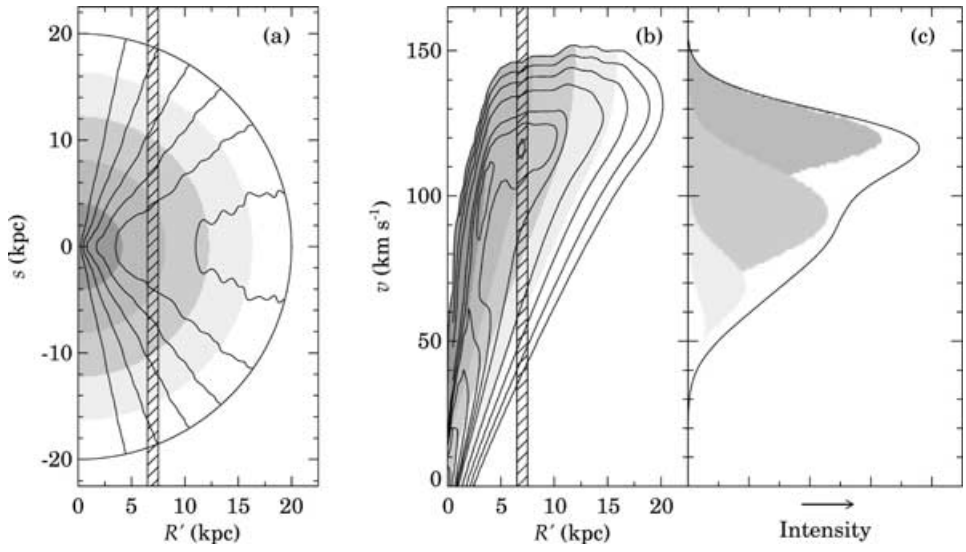

Figure 1. The mapping of the gas density and kinematics on to the XV plane, illustrated for a simulated edge-on view of the H I in NGC 2403 (adopted distance 3.2 Mpc). (a) Spider diagram showing the line-of-sight velocities in the disc plane (receding side only). Contours range from 10 to 130 km s^{-1} in steps of 20 km s^{-1}. The grey-scale divides the plane into a set of five rings, uniformly spaced in radius. (b) The integrated major axis position–velocity diagram in contours. The grey-scale indicates the rings in the disc plane from which the H I originates. (c) A velocity profile (solid line) at a projected radius of 7 kpc (the hatched region in the other panels) and the contributions from the different rings (grey-scale).

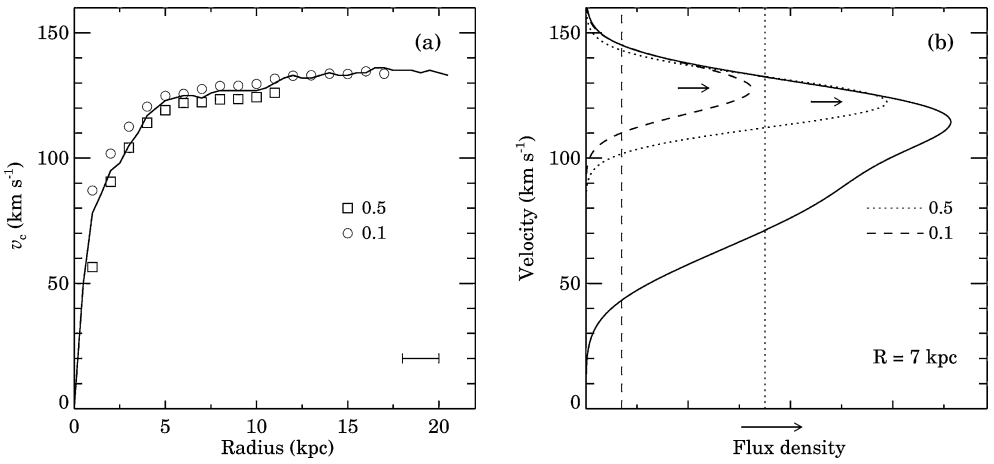

Figure 2. The envelope-tracing method applied to a simulated edge-on XV diagram of NGC 2403, illustrating that the inferred rotation curve differs from the true curve and depends on the data quality. (a) Comparison of the velocities found by tracing the envelope (symbols) with the true rotation curve (solid line). Squares/circles show the results of the Gaussian fits that include emission down to a level of 0.5/0.1 times the peak emission. The bar indicates the beam size. (b) The envelope fits (dashed and dotted Gaussians) for a single velocity profile at a projected radius of 7 kpc (solid line). The vertical lines show the level down to which emission was included in the fits, and the arrows indicate the inferred peak velocities.

gas at the line of nodes. An envelope-tracing technique can then be used to retrieve the rotation curve (Sancisi & Allen 1979).

The application of the envelope-tracing method to artificial data of axisymmetric H I layers in perfect circular rotation indicates that it works reasonably well at large projected radii (García-Ruiz et al. 2002). The reason is that at those radii the rotation curve is approximately flat, such that the extreme-velocity envelope of the XV diagram is only mildly contaminated by beam smearing (i.e. the presence in a single velocity profile of emission from neighbouring positions due to the finite spatial resolution) and line-of-sight projection. There is, however, a small systematic error introduced by the fact that the envelope is not solely due to the H I at the line of nodes, as assumed. Instead, the envelope also contains emission from the high velocity tails of H I clouds located in front of and behind the line of nodes (but seen in projection). This H I causes the high velocity side of the observed line profiles to deviate from an exact Gaussian tail with dispersion $\sigma_{\rm H\,I}$ (cf. Olling 1996). The strength of this deviation mainly depends on the H I surface density distribution. Consequently, the result of the envelope-tracing method depends on the part of the envelope included in the fit.

The effect is illustrated in Fig. 2 for the simulated edge-on view of the intermediately inclined spiral NGC 2403 (see Fig. 1). The use of upper fitting boundaries at relatively low velocities, as would be used in case of poor signal-to-noise ratio data, yields rotation velocities that are systematically lower than the true rotation (squares). High upper fitting boundaries on the other hand clearly yield velocities which are systematically higher than the true rotation (circles). Although this error is relatively small at large radii, reaching values of $\sim$5 km s^{-1}, it is systematic. More importantly, at small projected radii the discrepancy can become much larger (Fig. 2). This additional effect is caused by beam smearing, which is contaminating the extreme-velocity side of the velocity profiles with emission from larger projected radii. The beam-smearing effect by itself leads to an overestimate of the rotational velocities at small projected radii (see also García-Ruiz et al. 2002). For poorly resolved edge-on spirals, the steepness of the inner rise of the rotation curves may thus be overestimated. Note that this is contrary to the underestimation of the rotation curves of less-inclined spirals that occurs when beam smearing is not taken into account in deriving the velocity field (Begeman 1987).

A possible solution to the fundamental problem of beam smearing in edge-on spirals is to fit Gaussians to the edges of the velocity envelope in the spatial direction as well, and adopt the minimum of both curves as the rotation curve (García-Ruiz et al. 2002). However, this approach does not take into account the fact that a large fraction of the emission at small projected radii is due to H I in the outer parts of the galaxy seen in projection. For example, the proposed method would assign rotational velocities at small radii even in the case of a central H I hole. Furthermore, the rotation curve derived from the gas at the line-of-nodes is not necessarily a global rotation curve (Irwin 1994). Below we propose a method in which the entire XV diagrams is modelled using the rotation curves derived in Paper II with the envelope-tracing technique as initial estimates. The new approach implicitly corrects for the effects of the line-of-sight projection and beam smearing and provides a more robust error analysis.

2.2 Fitting the full XV diagram

The important property of the line-of-sight projection is that each ring or annulus in the disc plane maps on to a straight line in the XV diagram. Hence, in the outskirts the velocity profiles are dominated by the H I from a small range in galactocentric radius (a single ring in Fig. 1a), whereas towards smaller projected radii, an increasing number of rings are seen in projection. The mapping of circular orbits on to the XV plane can be inverted by modelling an observed XV diagram with a set of concentric, coplanar rings using an outside–in or 'onion peel' approach. Assume that the dynamical centre and systemic velocity are known. On one side of the galaxy (receding or approaching) consider first the velocity profile at the outermost projected radius where gas is detected, $R'_{\rm outer}$. When the surface density profile is known, e.g. using Warmels' (1988) method (see also Paper II), and assuming that the gas velocity dispersion is constant throughout, the rotational velocity at $R_{\rm outer}$ can be determined in a fit of equation (1) to the outermost velocity profile. For the initial estimate the velocity obtained with the envelope-tracing method can be used. Following this first fit the neighbouring profile at smaller projected radius is considered, $(R'_{\rm outer} - \Delta R')$. Here $\Delta R'$ is the adopted width of the rings (or annuli). At this point the velocity profiles at $R'_{\rm outer}$ and $(R'_{\rm outer} - \Delta R')$ are fitted simultaneously. As initial estimates the value of the rotational velocity

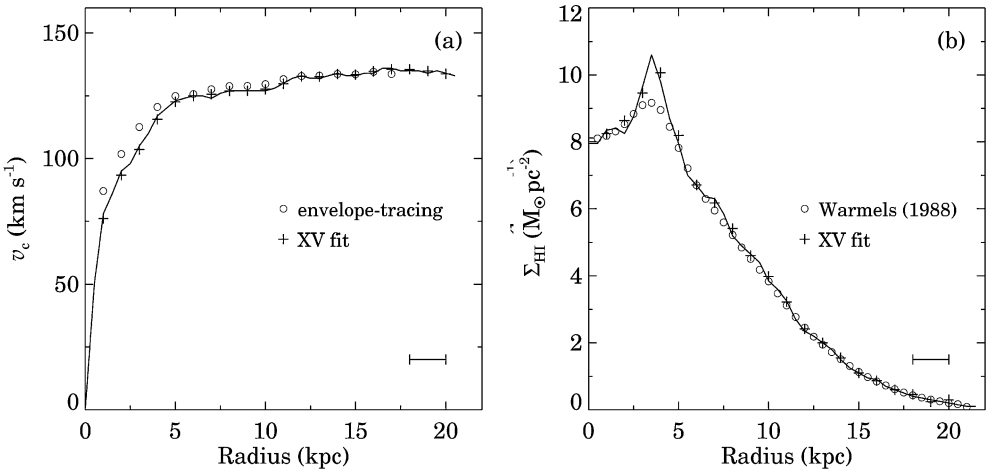

Figure 3. Results of the application of 'XV fit' to the simulated XV diagram of NGC 2403 (Fig. 1). (a) Rotation curve (crosses). Circles denote the curve obtained with the envelope-tracing method, for which the fits included emission down to a level of 0.1 times the peak emission. (b) Surface density profile (crosses). Circles denote the profile obtained with Warmels' (1988) method. In both panels, the solid lines denote the true curves (Fraternali et al. 2002). The bars indicate the beam (FWHM).

determined in the previous fit is used at $R'_{\rm outer}$ and at $(R'_{\rm outer} - \Delta R')$ the envelope-tracing value is taken. In this way the part of the XV diagram at and outside the current projected radius is fitted, yielding the velocity at the current radius, $v_{\rm c}(R_{\rm outer} - \Delta R)$ and a new value for $v_{\rm c}(R_{\rm outer})$. This procedure is repeated for the neighbouring line profile in the diagram $(R'_{\rm outer} - 2\Delta R')$ until the centre is reached.

Such an outside–in approach to fitting the XV diagram does not become ill-constrained. The reason is that the information included in the fit increases at the same rate as the number of free parameters (with one parameter for each new position) and in general the signal-to-noise ratio increases with decreasing radius. In addition to fitting the rotation curve it is also possible to simultaneously fit the surface density profile. However, this doubles the number of free parameters and is only justified for high signal-to-noise ratio data (Section 2.3). Letting the velocity dispersion free is stretching the data too far. Note that this XV fitting method can also be applied to galaxies of lower inclination, as long as the XV diagram is obtained by integrating along the minor axis.

Beam smearing can be naturally included by fitting a smoothed model. In that case a model velocity profile is easily constructed by first calculating a sufficient number of adjacent velocity profiles using equation (1). This 'mini' XV diagram surrounding the requested velocity profile is then convolved along the spatial axis with a Gaussian beam representative of the observations. The beam smearing corrected velocity profile is retained for use in the χ^2 fitting. Similarly, the effects of the instrumental bandwidth and a Hanning taper can be mimicked by convolving the model velocity profile.

The minimization of χ^2 is handled well by the 'amoeba' implementation (Press et al. 1992) of the simplex method (Nelder & Mead 1965). The simplex method is suitable because (i) it can easily handle a large number of free parameters and (ii) it does not require the derivatives of the model with respect to those parameters (a calculation of which would need an excessive amount of computing time). Errors can be estimated using Monte Carlo simulations (Section 2.3).

As an example, consider the simulated H I XV diagram of NGC 2403 presented earlier (Fig. 1). To highlight the effect of beam smearing, this XV diagram was smoothed to a spatial resolution of 2 kpc (full width at half maximum, FWHM). For an initial estimate of the rotation curve the envelope-tracing method was used with a fitting boundary at high velocities. For the surface densities initial estimates were obtained using Warmels' (1988) method. The XV-fitting technique was then applied as outlined above, letting both the rotation curve and density profile free in each of the fits. The result is shown in Fig. 3. The XV-fitting method is able to accurately retrieve both the rotation curve and surface density profile, in contrast to the methods used to obtain the initial estimates. The envelope-tracing method systematically overestimates the rotational velocity, especially in the inner region. This overestimation is an artefact caused by a combination of beam smearing and the choice of the upper fitting boundary. Note that the envelope-tracing method would have underestimated the rotation curve when a fitting boundary was chosen at relatively low velocities, as in case of poor signal-to-noise ratio data (cf. Fig. 2). Beam smearing is also the cause of the fact that Warmels' (1988) method (Fig. 3b, circles) is unable to retrieve features in the surface density profile smaller than the beam size. This is most clear for the peak of the density profile, which is smoothed out in Warmels' (1988) method, but is retrieved by the XV-fitting method.

In short, fitting the entire XV diagram as described here has several advantages. The most fundamental one is the correction for the effects of beam smearing and the line-of-sight projection. In addition, all the information available in the XV diagram is used. These advantages apply especially to the inner (rising) parts of the rotation curve, for which current H I synthesis observations are characterized by poor spatial resolution in all but the nearest galaxies. Of course, the applicability of the XV fitting method is limited inherent to the assumptions of axisymmetry, transparency and pure circular rotation. The XV diagram of the residuals, left after subtracting the model from the observations, provides information regarding deviations from these assumptions.

2.3 Tests on artificial position–velocity diagrams

Monte Carlo simulations are a useful tool for establishing the convergence of the XV-fitting method in the presence of noise. These simulations can also be used to study the applicability of the method with respect to different rotation curve shapes and beam sizes and to quantify the random errors of the derived rotation curves.

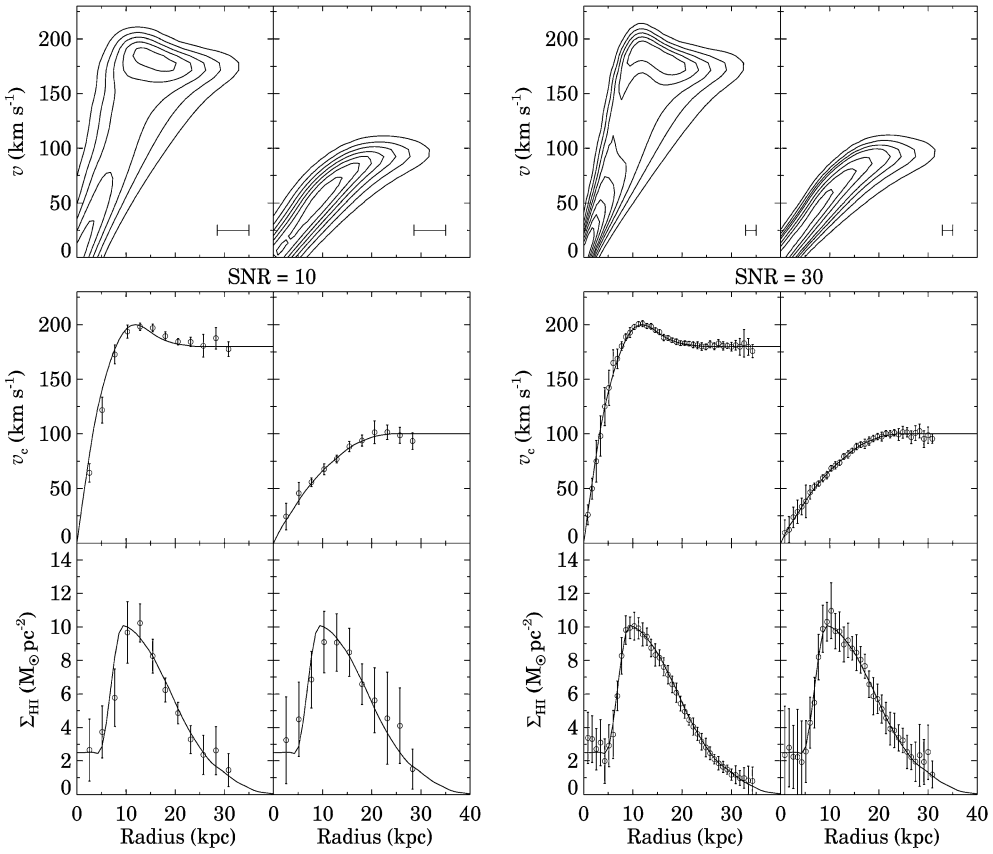

Figure 4. Results of Monte Carlo simulations of the XV-fitting method for two different rotation curve shapes, at a peak S/N ratio of 10 and a large beam size (left) and at a peak S/N ratio of 30 and a small beam size (right). Top panels show the noiseless artificial XV diagrams in contours. The beam size is indicated in the lower right. Middle panels show the mean (circles) and the 1σ dispersion (error bars) of the fitted rotational velocities for each ensemble. Bottom panels show the results for the surface densities. Solid lines show the true rotation curves (middle panels) and density profiles (bottom panels).

To assess the XV-fitting method in the presence of noise two artificial XV diagrams were created using equation (1) with $\sigma_{\rm gas}$ constant at 10 km s^{-1}. For the first a steep rotation curve with a local maximum was chosen, characteristic of those observed in massive high-surface-brightness spirals, whereas a slowly rising rotation curve characteristic of low-surface-brightness (LSB) spirals was used for the second. In both cases the same surface density profile was used, having an exponential decline at large radii and a strong depression at small radii. Fig. 4 illustrates the XV diagrams (top panels). For each artificial XV diagram two ensembles of 20 noise realizations were created using Gaussian random deviates. The first ensemble has a 1σ noise level corresponding to a ratio of the peak signal-to-noise ratio of 10 (S/N = 10) and a large beam size, typical of poor quality observations. The second used a peak S/N ratio of 30 and a small beam size, mimicking good quality observations. In each of these XV diagrams the emission was isolated by discarding the signal below a level of 2σ and manually removing the remaining noise peaks.

The initial estimates were derived using the envelope-tracing method for the rotation curve and Warmels' (1988) method for the surface density profile. The receding sides of the artificial XV diagrams were then fitted as described in Section 2.2, letting both the rotation curve and surface density profile free. In each fit the simplex search of parameter space was terminated at the point when it yields a less than 10 per cent decrease in χ^2.

The results of the fits for the ensembles of artificial XV diagrams are illustrated in Fig. 4. The figure reveals several interesting points. First and foremost, the XV-fitting method is able to recover the true rotation curves and density profiles to within the dispersion, both at low S/N ratio and large beam size and high S/N ratio and small beam size. The dispersion in the velocities decreases with increasing S/N ratio and decreasing beam size, although the effect is not very large for the S/N ratios and beam sizes chosen (a factor of 1.5–2). The dispersions are somewhat larger for the LSB model, which is probably due to the fact that a slowly rising curve causes the individual rings to overlap in the XV plane. At low S/N ratio, however, the rotational velocities still show a systematic offset from the true curve. In this case the data do not provide sufficient constraints to improve upon the initial estimates. Somewhat better results for the rotation curve are obtained when the surface density profile is kept fixed at its initial estimate, but in general the S/N ratio of 10 is simply insufficient. The simulations also reveal a side-effect at the outermost points. At the edge of the XV diagrams, defined by the 2σ level, the surface densities are slightly overestimated due to the presence of a small amount of signal from larger galactocentric radii (which was assumed to be zero). This leads to a small underestimate of the fitted rotational velocities at those radii.

It is important to stress the need for reasonable initial estimates. Tests which instead used initial estimates created by adding random offsets to the true curves indicate that the initial estimates for the rotational velocities need to be within $\sim$20 km s^{-1} from the true values. This accuracy may prove difficult to reach in the inner rising part of the XV diagram where the envelope-tracing method cannot

provide good initial estimates. In that case, one may have to resort to a manual approach.

3 ANALYSIS

3.1 The sample

The sample of edge-on galaxies to which the XV fitting method was applied is listed in Table 1. These galaxies were selected from Paper II by requiring the peak S/N ratio in the integrated H I XV diagram to be at least 10 (see Paper II for details on their construction). To meet this condition, the XV diagrams of several galaxies were Hanning smoothed in velocity. NGC 891 was added to this sample, using the Westerbork Synthesis Radio Telescope H I observations of Swaters et al. (1997). Its integrated XV diagram was extracted using the stellar disc centre and position angle (table 4 in Paper I). To avoid including the H I attributed to the halo (Swaters et al. 1997) the vertical integration was stopped at a distance of 20 arcsec from the plane. Notable features of NGC 891 are that it is only slightly warped (Rupen 1991; Swaters et al. 1997), and that its southern H I extension may be located far from the line-of-nodes or be in non-circular motion (Sancisi & Allen 1979; Rupen 1991).

3.2 Remaining concerns

Before applying the XV fitting method, it was investigated to what extent the assumption of transparency in the H I line holds. In Paper II it was already noted that the continuum emission and hence the continuum absorption is negligible. For NGC 891, however, substantial absorption against the strong radio continuum is likely (Sancisi & Allen 1979). Therefore, the XV fits for NGC 891 will be treated differently (Section 3.3). In addition, the central region of the XV diagrams may be affected by significant H I self-absorption due to velocity crowding. To check this assertion, the maximum optical depth in the channel maps was estimated according to $\tau_{\max} = -\ln[1 - T_B(\max)/\langle T_{\rm spin}\rangle]$, where $T_B(\max)$ is the maximum brightness temperature in the channel maps and $\langle T_{\rm spin}\rangle$ is the mean spin temperature. According to studies of H I absorption spectra for individual sightlines within the Milky Way and towards M31 and M33 the mean spin temperature is in the range 130–450 K, with the higher values corresponding to the outer parts of the galaxies (Dickey & Brinks 1993 and references therein). For edge-on systems it is thus expected that the mean spin temperature varies considerably along the line of sight and hence across the XV diagram. Therefore, the maximum optical depths were calculated for a conservative constant $\langle T_{\rm spin}\rangle$ of 100 K. The results, listed in Table 1, imply optical thinness for all of the spirals in the sample except NGC 891.

Another concern is that the inclination and position angles are assumed constant with galactocentric radius. This is not a problem in the region of the stellar disc, where the H I layer is close to being coplanar (Briggs 1990; Bottema 1996). However, beyond the stellar disc the H I layer is often warped (Sancisi 1976; Bosma 1991; Christodoulou, Tohline & Steiman-Cameron 1993; García-Ruiz, Sancisi & Kuijken 2002), showing warping angles of up to 30° (Bottema, Shostak & van der Kruit 1987). Fortunately, for the spirals in the present sample the H I does not extend far beyond the stellar disc and contains no such strong warps (fig. 3 in Paper II). Still, since many do clearly show moderate warping, the effect of a warped H I layer on the observed XV diagram should be considered. Briefly, for an H I layer of which the inner region is coplanar and edge-on, the line-of-sight velocities of an outer tilted ring are lower compared with those expected for a coplanar ring. The difference in line-of-sight projected velocity between a tilted ring and a coplanar ring is maximal at the ascending node in case the ascending node coincides with the major axis. For an extreme warping angle $w = 30°$ the velocity is lowered by $(1 - \cos w)$ or 13 per cent. It can be concluded that the effect of a warp on the major axis XV diagram is significant only in case when the warping angle is large. Except for NGC 5529, the observed warps appear to be rather moderate such that the effect on the observed XV diagrams is likely to be unimportant.

3.3 Results

The emission in the XV diagrams was isolated by discarding the signal below a level of 2σ and manually removing the remaining noise peaks. The XV fits were then started at the outermost radius for which the velocity profile contains at least four independent data

Table 1. Properties of the XV diagrams and the XV fits.

Galaxy	Beam (arcsec)	Vel. res. (km s^{-1})	$\sigma_{\rm XV}$ (mJy beam^{-1})	S/N ratio	Mode	$\chi^2_{\rm rece}$	$\chi^2{}_{\rm appr}$	$\tau_{\max}$
(1)	(2)	(3)	(4)	(5)	(6)	(7)	(8)	(9)
ESO 142-G24	29.3	6.6	3.8	15	v	2.1	0.9	0.47
ESO 157-G18*	29.5	6.6	5.0	12	–	–	–	0.58
ESO 201-G22	27.8	13.2	1.9	15	v	0.8	2.1	0.20
ESO 240-G11	33.7	13.2	1.3	37	v+d	4.2	3.7	0.29
ESO 263-G15	25.6	13.2	1.7	19	v+d	1.6	1.6	0.31
ESO 269-G15*	33.2	13.2	2.3	14	–	–	–	0.23
ESO 416-G25*	50.7	13.2	2.2	12	–	–	–	0.10
ESO 435-G14*	34.4	13.2	2.7	12	–	–	–	0.23
ESO 435-G25	19.1	13.2	1.8	27	v+d	4.6	3.3	0.26
ESO 435-G50*	29.5	13.2	2.1	13	–	–	–	0.23
ESO 564-G27	69.9	6.6	4.0	36	v	2.0	2.1	0.38
NGC 891	20.0	33.0	0.31	148	v+d	60	134	0.85
NGC 5170	46.7	13.2	2.2	38	v	2.8	3.5	0.41
NGC 5529*	17.5	33.0	0.3	60	–	–	–	0.33

Columns: (1) galaxy, an asterisk indicates the XV fit did not converge; (2) spatial resolution in the integrated XV diagram (FWHM); (3) velocity resolution (FWHM); (4) noise level (1σ); (5) peak signal-to-noise ratio; (6) v+d, set free both the rotation curve and surface density profile in the fit, v, set free the rotation curve only; (7) and (8) reduced χ^2 at the receding and approaching side, respectively; (9) estimated maximum optical depth (see the text).

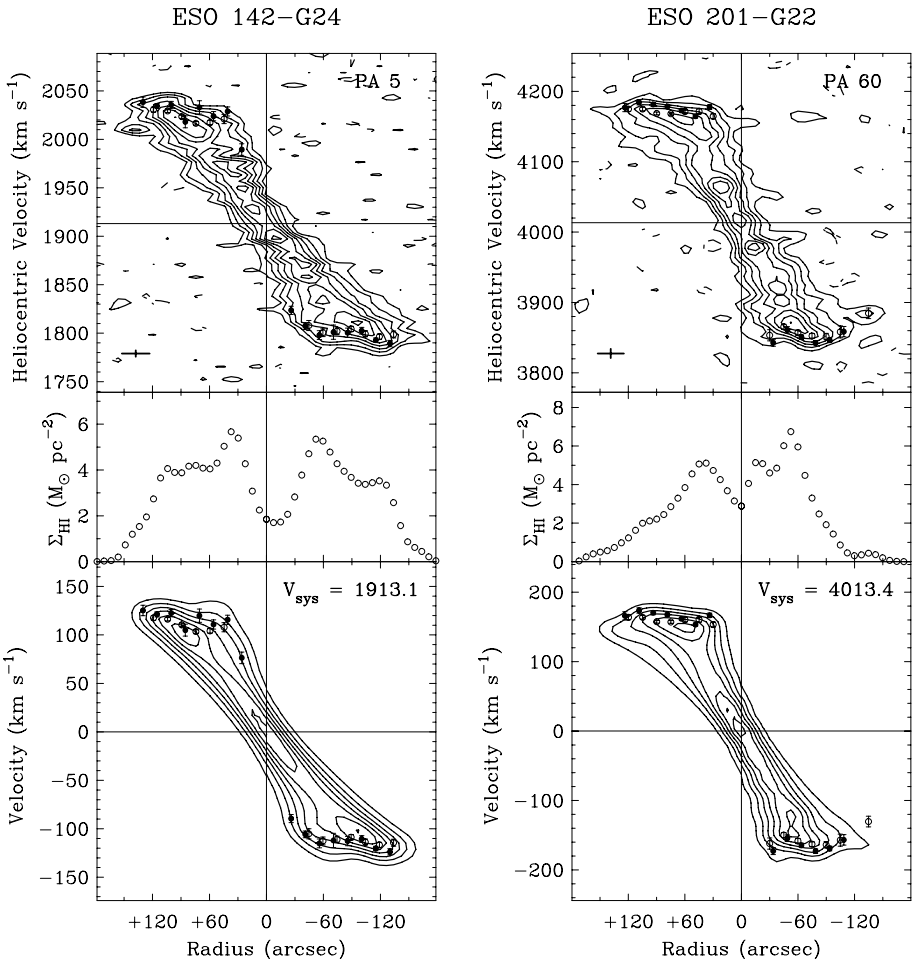

Figure 5. Results of the XV fits. Top, H I rotation curves (dots) overlayed on the observed XV diagram (contours). Contour levels are −4, −2, 2, 4, 6, 8, etc. in units of σ_{XV} (Table 1), except for ESO 240-G11, ESO 435-G25, ESO 564-G27 and NGC 5170 for which the levels are −4, −2, 2, 4, 8, 12, 16, etc. times σ_{XV}. Circles denote the velocities obtained with the envelope-tracing method. The cross in the lower right shows the resolution. Middle, H I surface density profile. Circles indicate the densities obtained using Warmels' (1988) method. The fitted density profile is also shown when letting it free significantly improved the χ^2 (dots). Bottom, as top but for the model XV diagram. Heliocentric velocities adhere to the radio definition except for NGC 891 where the optical definition is used.

points. The H I velocity dispersion was kept constant at 10 km s^{-1} and the systemic velocity was fixed at its value determined from the H I global profile (table 3 in Paper II). For NGC 891 v_{sys} = 528 km s^{-1} was used (Sancisi & Allen 1979). For the dynamical centre the stellar disc dynamical centre was taken (table 4 in Paper I), and the width of the rings was set to the pixel size. Each side of the XV diagram was fitted using as initial estimates the rotational velocities obtained with the envelope-tracing method and the density profile using Warmels' (1988) method. At the inner, rising part of the XV diagram initial estimates of the rotational velocities were obtained by linearly extrapolating the envelope-tracing velocities to the dynamical centre. The XV fits were performed both for a free and a fixed density profile, and the best fit in terms of reduced χ^2 was retained. In the cases in which a Hanning taper was used with the observations the model velocity profiles were smoothed accordingly. For each galaxy a series of XV diagrams of the residuals, constructed by subtracting one by one each of the individual fitted rings from the observed XV diagram, was inspected to determine the smallest galactocentric radius at which H I is detected. The derived rotation curves and (in a few cases) the surface density profiles were averaged to yield roughly two points per beam (FWHM).

The successful fits are illustrated in Fig. 5 and their properties are listed in Table 1. The errors were calculated using the Monte Carlo approach (Section 2.3). In six cases the fits did not converge. For ESO 269-G15, ESO 416-G25, ESO 435-G14 and ESO 435-G50 the XV diagrams are of particularly poor spatial resolution and signal-to-noise ratio (S/N < 15), which has probably caused the XV fitting method to diverge. For the other two systems the assumption of axisymmetry clearly does not hold. ESO 157-G18 is a dwarf system that is strongly lopsided (see notes in Paper II). NGC 5529 is a massive, spiral with a pronounced warp in H I. In the following, the results for each of the successful fits will be described.

ESO 142 -G24. The XV fits show that H I emission is present down to a galactocentric radius of 25 arcsec, thereby revealing the rising part of the rotation curve. The residual XV diagram, left after subtracting the best-fitting model, does not show any obvious structure. Receding side, at radii less than 60 arcsec the XV fit velocities are 5–15 km s^{-1} higher than those derived from the extreme velocity envelope. Approaching side, a good fit, the XV fit velocities are consistent with the earlier envelope-tracing results.

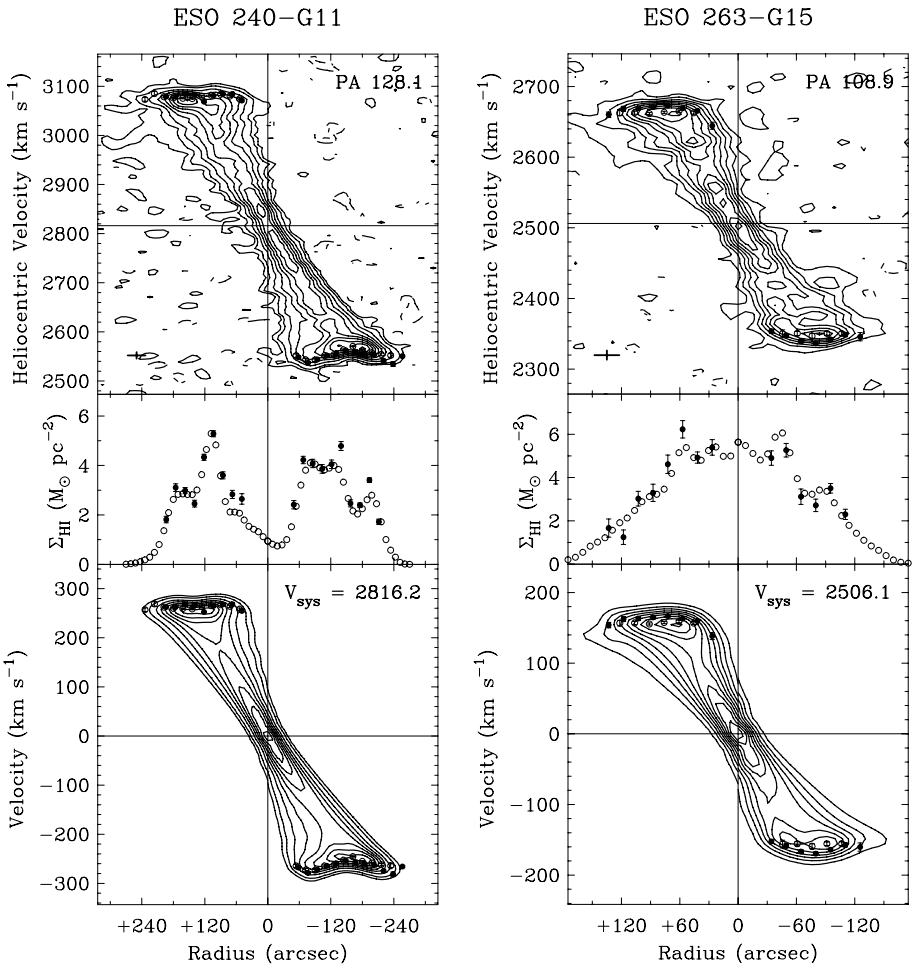

Figure 5 – *continued*

ESO 201-G22. Receding side, the residuals are comparable to the noise. Remarkably, at radii beyond 60 arcsec the XV fit velocities are up to 20 km s^{-1} higher than those obtained with the envelope-tracing method. Approaching side, the 'ridge' structure at a radius $R \sim -40$ arcsec is difficult to reproduce with the model. XV fit velocities are up to 10 km s^{-1} higher than the envelope-tracing velocities.

ESO 240-G11. Letting the density profile free reduces χ^2 by a factor of 2. The XV diagram of the residuals reveals a lack of H I at radii smaller than 40 arcsec. The observed XV diagram does appear to show emission at $R \sim -20$ arcsec and a velocity of -270 km s^{-1}. Receding side, the velocities agree well with the earlier envelope-tracing results. At the outermost radii the fits do not give a meaningful result because of the large range in velocity covered by the faint emission. The ridge structure at $R \sim +100$ arcsec is not well reproduced. Approaching side, results agree to within 5 km s^{-1} with the envelope-tracing results except for the outermost radii. The latter may be caused by the edge-effect (Section 2.3).

ESO 263-G15. The symmetric XV diagram is very well reproduced by the model. The fitted rotational velocities are $\sim$10 km s^{-1} higher than the envelope-tracing velocities. Receding side, the residual XV diagrams reveal H I down to $R \simeq +25$ arcsec.

ESO 435-G25. The XV diagram is highly asymmetric. The residual XV diagrams show a lack of H I at $R \lesssim 50$ arcsec. Receding side, the upturn in the velocities at large radii is associated with the (projected) end of the curved ridge dominating the XV diagram on this side. Approaching side, the XV fit velocities are slightly higher than those derived from the envelope. Interestingly, the velocities in the extension ($R > 180$ arcsec) are higher than those found with the envelope-tracing method, but consistent with a flat rotation curve. The extension is similar in appearance to the well-studied southern extension of NGC 891 (Rupen 1991).

ESO 564-G27. The residuals are comparable to the noise. The XV fit velocities are consistent with the envelope-tracing method.

NGC 891. For NGC 891 a different approach was taken in order to minimize the influence of the probable absorption. Here, each velocity profile was fitted separately, such that once the circular velocity is determined at a certain radius it is kept fixed in each of the remaining fits. This ensures that the fit is less susceptible to absorption because the inner part of the XV diagram, where the absorption is probably highest, no longer influences the determination of rotational velocities at larger radii. The resulting fit matches the extreme-velocity envelope very well. The amplitude of the rotation curve is approximately 225 km s^{-1}, in agreement with previous H I studies (Sancisi & Allen 1979; Rupen 1991). The inner maximum is in agreement with the CO measurements (Sofue 1996). The decline of the rotational velocity at the onset of the southern extension ($R \sim +300$ arcsec) is much more gradual than it appears from the lowest

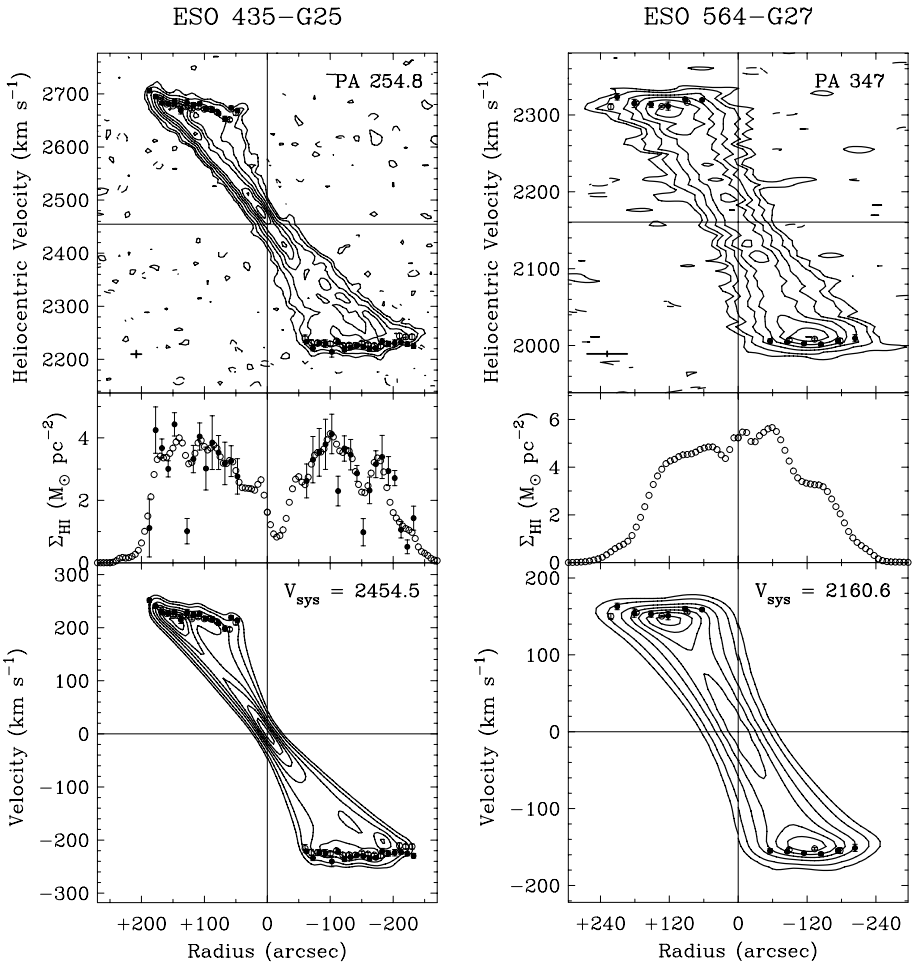

Figure 5 – *continued*

contour. This is caused by the sharp drop in H I surface density at that radius.

NGC 5170. Receding side, the XV fits did not converge at large radii, where the H I data indicate a double peaked velocity profile. The model does not reproduce the curved ridges that dominate both sides of the XV diagram in detail.

The assumption of pure circular motion can be checked at the minor axis. There radial motions will show up most clearly, broadening the velocity profile. Radial motions can thus be inferred by comparing the observed and model velocity profiles at the minor axis. Such a comparison is allowed because the XV fits were not performed all the way to the minor axis. A comparison of the widths of the minor axis velocity profiles shows that in none of the spirals the observed central velocity profile is significantly broader than that of the model. Any deviations from non-circular motion are therefore small and do not affect the analysis.

In several cases the rotational velocities found from the XV fits differ significantly from those determined using the envelope-tracing method. A clear example is ESO 263-G15, an Sc galaxy with a closely symmetric XV diagram but for which the envelope-tracing velocities are systematically lower by $\sim$10 km s^{-1}. This difference is likely to be due to the neglect of the effect of the line-of-sight projection of the envelope-tracing method and its sensitivity to the adopted fitting boundary. This would mean that our new method has successfully overcome these drawbacks of the envelope-tracing method.

In two cases, ESO 142-G24 and ESO 263-G15, the XV fits have provided information regarding the rotation curve at small radii that could not be obtained with the envelop-tracing technique. In these cases our method also has extended and improved the analysis in terms of deriving a rotation curve from the observations.

In general, however, the analysis has not provided the anticipated information on the inner parts of the rotation curves. In several cases this lack of information at small galactocentric radii is caused by an H I deficiency; nearly all of the emission observed at small projected radii is due to H I at large galactocentric radii seen in projection. The clearest examples are ESO 240-G11, ESO 435-G25 and NGC 5170. The fact that this H I deficiency is not apparent in the face-on density profiles derived using Warmels' (1988) method is probably due to the well-known fact that this method overestimates the H I surface density in the central parts (Warmels 1988; Swaters 1999). In other cases, poor spatial resolution further prevents an analysis at small galactocentric radii (ESO 201-G22 and ESO 564-G27). In the following section the H I results will be combined with the kinematical information from the optical emission lines to further investigate the rotation curves in the inner parts. Although the new method has not been able to derive rotation velocities at smaller radii, it has on the other hand shown more reliably that such information is not present in the data

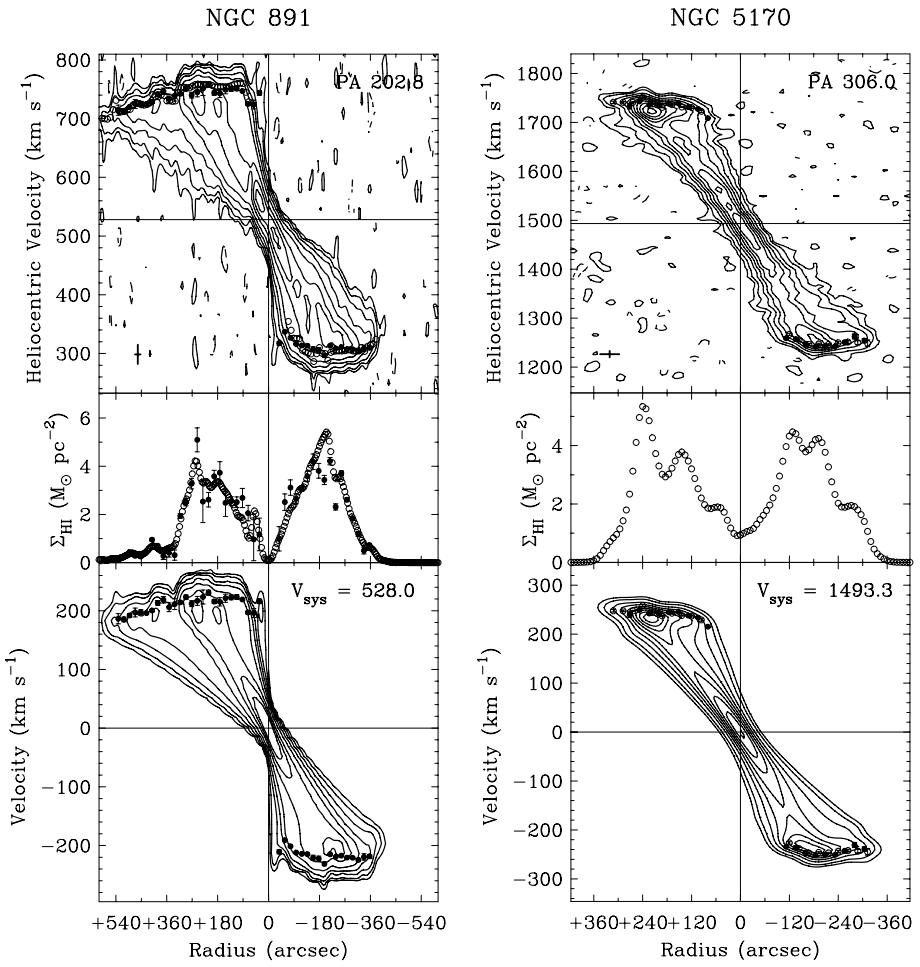

Figure 5 – *continued*

either because of the absence of H I at these radii or due to poor resolution.

4 OPTICAL EMISSION LINE KINEMATICS

The optical emission lines of spiral galaxies can be studied at high spatial resolution and provide extra information concerning the rotation curve at small radii. Unlike the H I, however, the optical emission lines are affected by dust extinction. If the filling factor of the dust is such that in the edge-on view the H II regions at the line of nodes are unobscured, then the full velocity range will be observed. When, on the other hand, the galaxy is completely optically thick only the galaxy outskirts will contribute to the velocity profiles, yielding an apparent solid-body rotation curve (Goad & Roberts 1981). In edge-on spirals, a comparison of the velocities derived from the optical emission lines with the H I rotation curve can thus be used to infer whether extinction is seriously affecting the optical velocity profiles (Bosma et al. 1992). Such a comparison is important not only for rotation curve studies, but also because dust extinction similarly affects the stellar kinematics.

Long-slit spectroscopic observations were performed for a sample of 19 edge-on spirals of intermediate to late morphological type (Paper I). Spectra were taken either in the 4800–5800 Å region, covering the Hβ and the [O III]5007 emission lines, in the 6000–7000 Å region, containing Hα, or in both wavelength regions. A detailed account of the observations and basic data reduction is given in Paper I. In the spectra of ESO 437-G62, ESO 487-G02 and ESO 509-G19 the optical emission lines remained undetected. To isolate the emission lines in the other spectra both the galaxy continuum and the stellar absorption lines were removed as follows. The absorption lines were modelled with the stellar template spectra used to determine the stellar kinematics. First, the stellar continuum of the template star was fitted using a low-order polynomial and removed through division. Then, for each position along the slit this template absorption-line spectrum was shifted and broadened according to the line-of-sight stellar kinematics. In essence, the resulting spectrum is a continuum-divided model of the galaxy absorption lines. Finally, this model was multiplied into the galaxy continuum, also determined by fitting a low-order polynomial, and subtracted. For ESO 263-G15 and ESO 435-G50 the stellar kinematics could not be determined (Paper I), and their continuum was instead removed by subtracting a low-order polynomial fit.

While well resolved spatially, the low spectral resolution and the patchy distribution of ionized gas preclude a correction for the effect of line-of-sight projection using the XV fitting method. The optical emission line kinematics were instead derived by fitting Gaussians to the velocity profiles (Goad & Roberts 1981; Makarov et al. 1997). In case of double-peaked velocity profiles, two Gaussians were used. The mean (peak) velocities of the best-fitting Gaussians are shown overlayed on the H I XV diagrams in Fig. 6. The best-fitting Gaussian

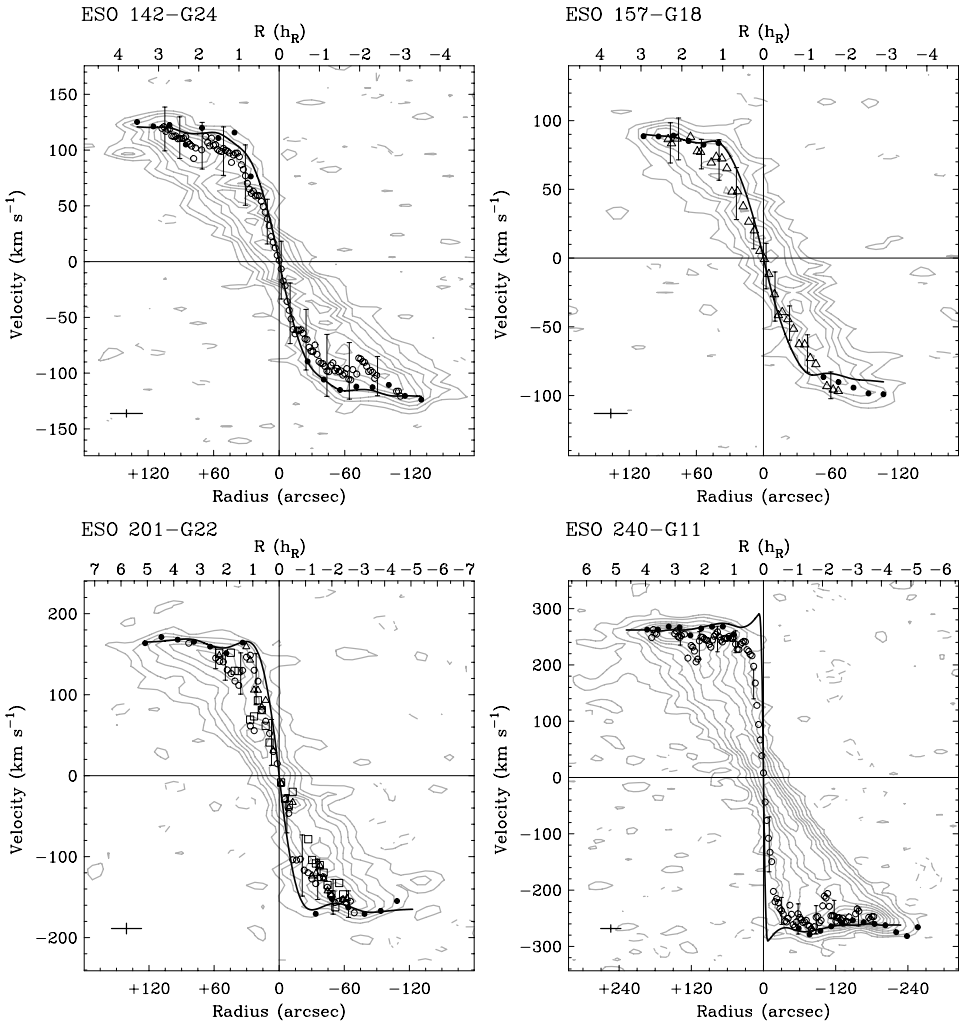

Figure 6. Optical emission line velocities overlayed on the H I XV diagrams for 16 galaxies. Circles, Hα; triangles, Hβ; squares, [O III]5007; crosses, Hα from Persic & Salucci (1995). The error bars indicate the H II velocity dispersion ($\pm$ 1σ). The dots show the H I rotational velocities and the solid line shows the adopted rotation curve (Section 5). H I contours are as in Fig. 4. For galaxies not part of Fig. 4 contour levels are as in fig. 2 of Paper II, except for ESO 435-G14 for which a Hanning smoothed version is shown using levels of -4, -2, 2, 4, 6, 8, 10, etc. times σ_{XV}. The cross in the lower left shows the H I resolution, and the top axis is in units of *I*-band disc scalelengths.

dispersions, corrected for the spectral resolution, are also shown (error bars, at a few radial positions for clarity). Where available, the Hα line was used to calculate the dispersions because of its higher brightness and the higher velocity resolution in the red. For the galaxies observed with VLT–FORS2 the Hβ line was used, except for ESO 435-G25 for which the [O III]5007 line is much brighter. Note that the systemic velocities of the H I and the optical emission lines are in good agreement. The symmetric rotation curves (solid lines) were obtained by averaging the H I rotational velocities at the approaching and the receding sides, and taking in the inner parts an estimate of the extreme velocities reached by the H II. For the latter the sum of the H II mean line-of-sight velocity and the H II line-of-sight velocity dispersion is adopted. The curves will be further discussed in Section 5. Here, the optical emission line kinematics, hereafter often referred to as simply H II kinematics, will be described for each galaxy.

ESO 142-G24. The H II velocity distribution extends up to the extreme-velocity envelope of the H I at all radii. In the outer parts the Hα closely traces the bright H I ridges. These ridges appear to coincide with spiral arms in the optical image, suggesting that the dip in the H II mean velocities at $\sim\pm$70 arcsec is due to the projection. The smooth connection of the Hα with the H I rotational velocities and the low galaxy inclination (table 1 in Paper IV) suggest that the effects of projection and dust extinction are small.

ESO 157-G18. The Hβ velocity distributions are consistent with the H I rotational velocities, except at ~ -60 arcsec. There, the Hβ velocities exceed the H I velocities by 10–15 km s^{-1}. The line-of-sight stellar velocities also show a disturbance on this side (fig. 5 in Paper I, see also Paper IV). The adopted rotation curve (solid line) pertains to the receding side.

ESO 201-G22. Although the slit covers part of the dust lane, the H II velocity distribution extends up to the H I rotation at most positions. This suggests that the effect of dust extinction on the H II kinematics is small. On both sides the H II velocity profiles are double peaked in the inner parts, tracing both the extreme H I velocities and a bright H I ridge.

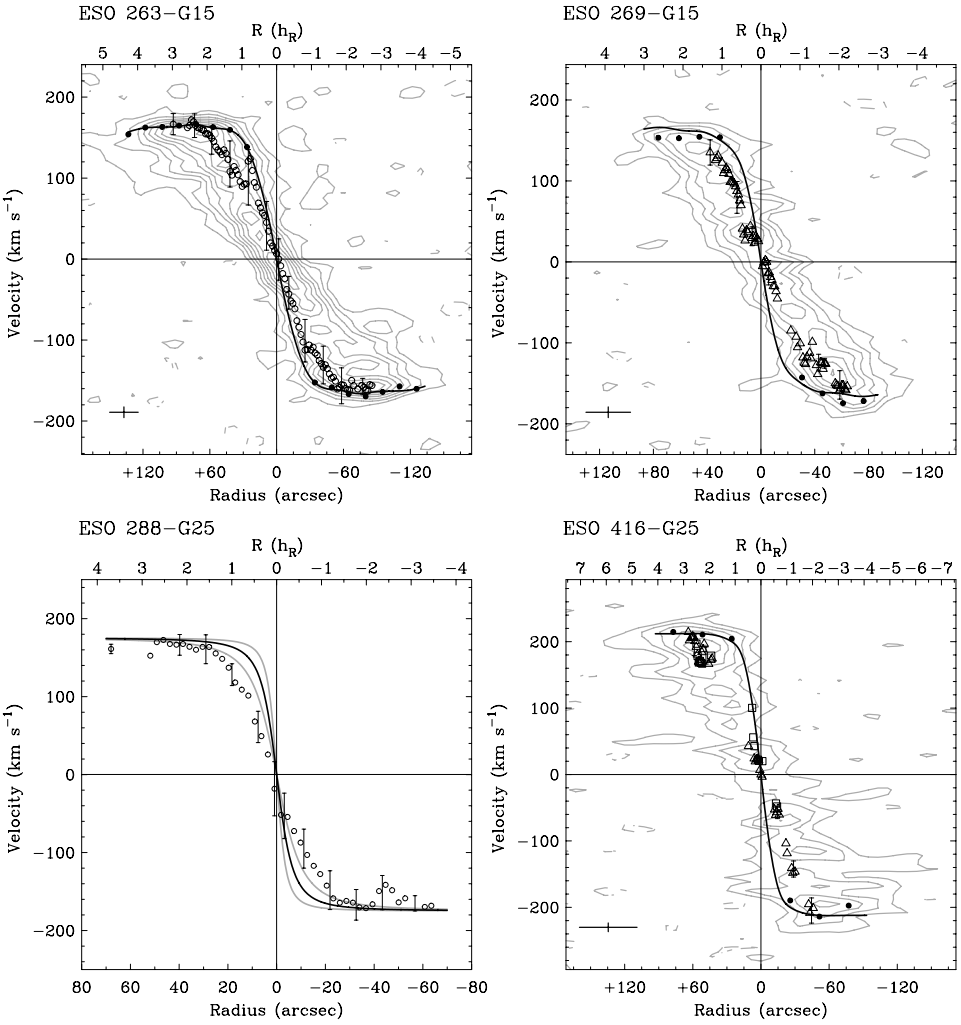

Figure 6 – *continued*

ESO 240-G11. The H II velocity broadening is much smaller than that of the H I. The observed Hα velocities are surprisingly close to the H I rotation down to a projected radius of 1 arcmin. At smaller radii Hα is clearly present, whereas H I is barely detected. In the innermost parts ($R \lesssim 5$ arcsec) the H II lines appear double peaked, showing the 'X' signature suggestive of a barred potential (see Fig. A1 and also Bureau & Freeman 1999). From 5 arcsec onward the velocities trace an apparent solid-body curve up to 15 arcsec. The inner maximum in the adopted rotation curve (solid curve) was chosen to match the H I and H II emission (see also Fig. A1).

ESO 263-G15. The Hα mean velocities of this virtually bulgeless Sc show a solid-body behaviour up to 25 arcsec, followed by a sharp drop and a steady rise to match the H I rotational velocities in the outer parts. On the receding side the drop is more pronounced and the Hα velocities reach the circular velocity further out (at 70 arcsec, versus 50 arcsec at the opposite side). While the galaxy is almost perfectly edge-on and shows a patchy dust-lane, the smooth connection of the H II velocity distribution with the H I rotational velocities at 30 arcsec suggests that in the inner parts the H II velocities are close to the true rotation curve. Note that the H II velocity broadening is smaller than that of the H I.

ESO 269-G15. The Hβ velocity curve is almost solid-body over much of its extent. The H II velocities are actually lower than the observed stellar velocities (Paper I). This is puzzling because the asymmetric drift is expected to be larger for the stars. Any dust extinction will also more strongly affect the stellar velocities because of the larger optical depth at shorter wavelengths. A possible explanation, although unexpected for a late-type spiral, is that the inner region is devoid of H II regions such that the H II emission at small projected radii is actually located in the outskirts of the disc.

ESO 288-G25. Although no H I information is available, the Hα reveals several important points. First, the Hα velocity distributions are consistent with a flat rotation curve beyond a radius of 20 arcsec. The systemic velocity, from symmetrizing the Hα velocities on the flat part, is 2495 km s^{-1} (optical velocity definition). The adopted rotation curve (solid line) is an 'eyeball fit' of the simple function $v(R) = v_{\rm max} R/\sqrt{R^2 + d^2}$, taking $v_{\rm max} = 175$ km s^{-1} and $d = 7$ arcsec. The grey lines show curves for $d = 4$ and 11 arcsec, and give an estimate of the uncertainty in the inner parts.

ESO 416-G25. The Hβ and [O III]5007 lines are faint for this closely edge-on Sb. The H II velocities agree with the H I rotation starting

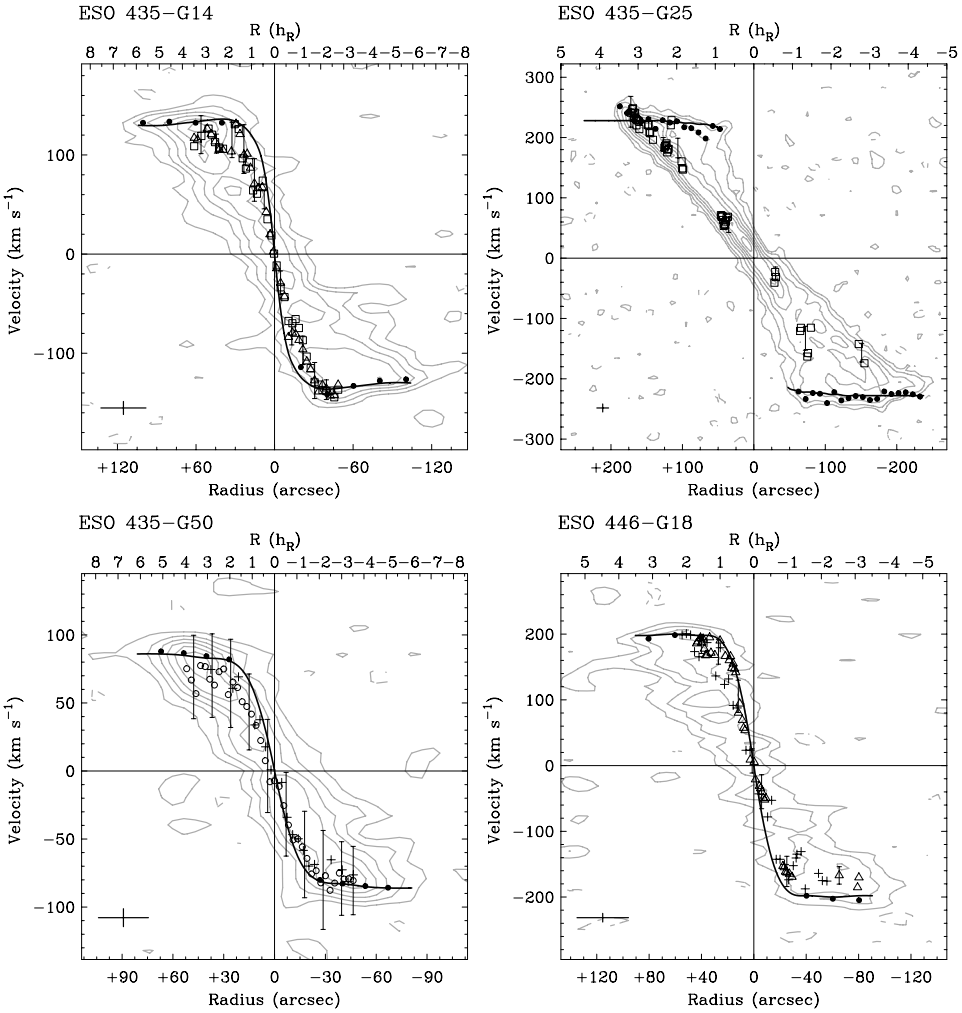

Figure 6 – *continued*

at radius of 40–50 arcsec, although the H I rotation curve itself is uncertain.

ESO 435-G14. The Hβ and [O III]5007 velocity distributions extend up to the extreme-velocity envelope of the H I at all radii. This indicates that the effects of dust extinction and projection are small, consistent with its low inclination ($i \simeq 82^\circ$, see Paper IV). The H II velocity broadening is smaller than that of the H I. This results from the low inclination and the fact that the H I beam is much larger than the Hα slit-width, so that line-of-sight effects are different for the two lines. The linear feature in the mean velocities on the receding side from $R \sim 50$ to $\sim$30 arcsec, coincides with a prominent spiral arm in the optical image (fig. A1 in KKG). No such feature is seen on the approaching side, where the H I emission is also much fainter.

ESO 435-G25. H II emission is mainly detected along the bright H I ridge that dominates the receding side of the H I XV diagram. This emission contains little information concerning the rotation curve. The rotation curve (solid line) cannot be determined in the inner parts.

ESO 435-G50. The Hα velocity distribution of this small Sc is consistent with the H I. Remarkably, the H II velocity broadening is approximately 30 km s^{-1} (1σ), similar to that of the H I.

ESO 446-G18. The Hβ emission line is weak, and the Hβ velocities were therefore complemented with the Hα velocities measured by Persic & Salucci (1995). The combined H II velocities show an apparent solid-body rotation within 20 arcsec, and agree with the H I rotational velocity further out. Outside 40 arcsec, the H II velocity distribution extends up to the extreme-velocity envelope of the H I.

ESO 564-G27. The H II kinematics show a pattern that is remarkably similar to that observed in ESO 435-G14. Both galaxies show an apparent solid-body rotation within 0.5 *I*-band disc scalelengths followed by a small plateau and a rise up to the H I rotational velocities at 1.5 scalelengths. Beyond that radius both galaxies show a dip in the mean velocities at 2 scalelengths (except for the approaching side of ESO 435-G14), followed by another increase to match the H I rotation curve at 3 scalelengths. Since the galaxies are both of type Sc and have a similar $v_{\rm max}$ (e.g. Table 2), this suggests that the effect of dust extinction is also small in ESO 564-G27.

NGC 891. For N891 the slit was placed at a distance of 10 arcsec from the plane, covering its approaching side out to 4 arcmin from the dynamical centre. The emission lines are well resolved in velocity, showing skewed velocity profiles. The lines were therefore also fitted using the Gauss–Hermite series (van der Marel & Franx 1993), including only the h_3 parameter. These fits reveal a prograde tail (i.e.

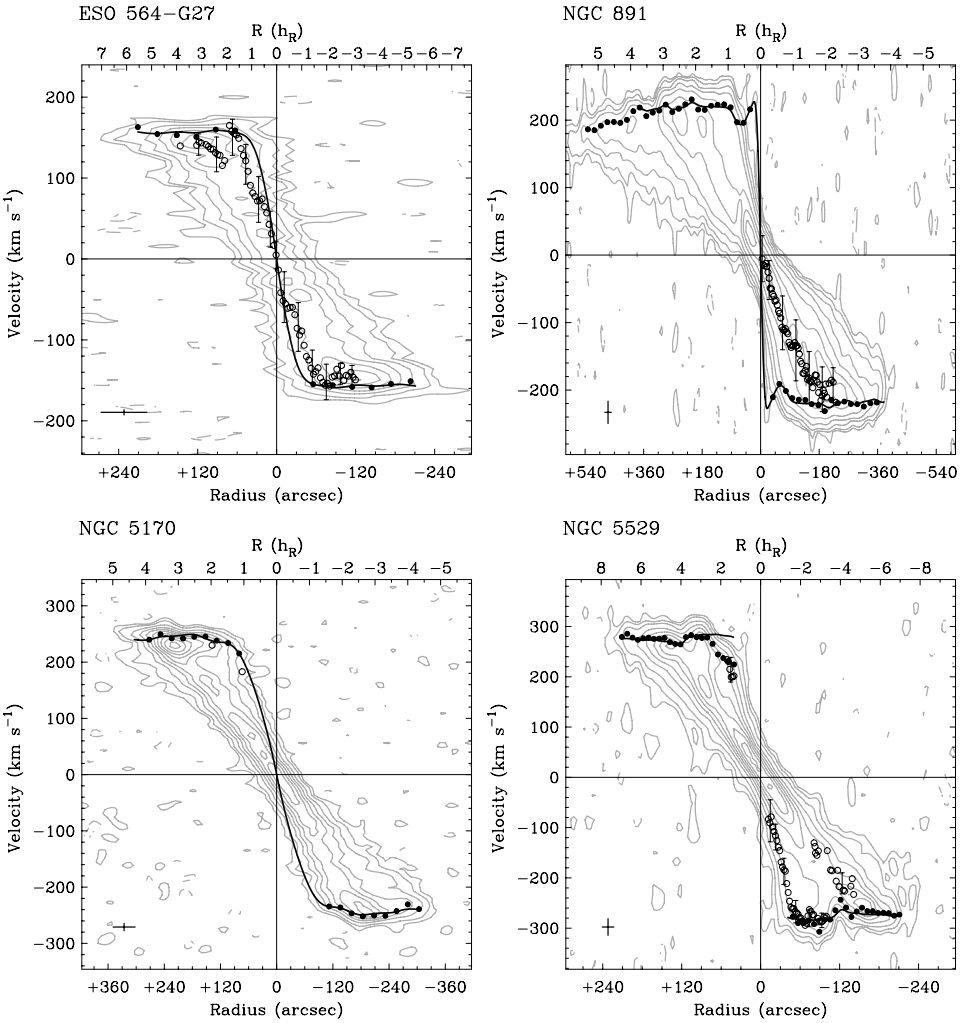

Figure 6 – *continued*

away from systemic) for radii up to 2 arcmin, with an average $h_3 \sim -0.03$. The stellar kinematics show a similar behaviour (see notes in Paper I). Beyond 2 arcmin the velocity profiles are indistinguishable from a Gaussian, and the Hα velocity distributions reach up to the H I rotation. The latter indicates that Hα emission is present at a galactocentric radius of 2 arcmin and that at 10 arcsec from the plane the disc is transparent. The observation that at 2 arcmin the Hα velocities fall short of the H I rotation at $z = 0$ (Bosma et al. 1992) therefore implies that at $z = 0$ the disc is still optically thick. Note that the adopted rotation curve does not include the southern extension ($R \gtrsim +6$ arcmin).

NGC 5170. For this galaxy the maximum Hα velocities in the two spectra taken perpendicular to the major axis are plotted. These extreme velocities occur exactly at the major axis and correspond to the H I rotation. This suggests that this massive Sc is transparent down to at least one *I*-band disc scalelength from the centre.

NGC 5529. The slit limits the observed radial range to (+1 arcmin, −3 arcmin) with respect to the dynamical centre. In the region of the peanut-shaped bulge the H II lines (Hα as well as [N II] and [S II]) show intricate double-peaked velocity profiles. These outline a 'figure-of-eight' signature with radius, indicative of a barred potential (see Fig. A1). In this region the rotation curve cannot be determined. At larger radii, the Hα mean velocities show a behaviour steeper than solid body up to ∼50 arcsec, after which they are consistent with the H I rotational velocities. In the outermost parts the profiles are again double-peaked. There the high velocity component traces the H I rotation, whereas the lower velocity component forms a linear feature which follows a bright H I ridge.

Table 2 does provide a firm handle on the effect of dust extinction at the exact slit positions studied. This will be taken into account when modelling the observed stellar kinematics (Paper IV).

5 DISCUSSION

The H I and H II kinematics provide two diagnostics for the dust opacity. First, an edge-on galaxy that is optically thick out to its periphery will show an apparent solid-body rotation curve in the optical regardless of the true rotation curve shape (Goad & Roberts 1981). None of the galaxies studied shows such an H II (Section 4) or stellar (Paper I) velocity curve. More specifically, in all cases for which both H I and H II kinematics are available the H II velocity distribution (H II mean velocity *plus* velocity dispersion) matches the extreme-velocity envelope of the H I at a projected radius between 1–2 *I*-band disc scalelengths. At this radius H II is detected

Table 2. Upper limits to the transparency radius.

Galaxy	Type	v_{max}	$\pm$	$R_{overlap}$	R_{slope}
		(km s^{-1})		($h_{R,I}$)	($h_{R,I}$)
(1)	(2)	(3)	(4)	(5)	(6)
ESO 142-G24	Scd	121	4	0.8	0.4
ESO 157-G18	Scd	88	6	1.1	0.4
ESO 201-G22	Sc	169	5	1.0	0.4
ESO 240-G11	Sc	273	7	1.2	0.4
ESO 263-G15	Sc	166	3	0.8	0.8
ESO 269-G15	Sc	167	8	1.7	0.9
ESO 288-G25	Sbc	175	5	–	0.7
ESO 416-G25	Sb	212	6	2.2	–
ESO 435-G14	Sc	136	9	1.4	0.6
ESO 435-G25	Sc	232	10	–	–
ESO 435-G50	Sc	86	4	1.9	0.9
ESO 446-G18	Sb	198	7	1.2	0.8
ESO 564-G27	Sc	160	6	1.3	0.5
NGC 891	Sb	227	5	1.3	0.8
NGC 5170	Sc	250	4	1.0	–
NGC 5529	Sc	284	8	2.0	1.3

Columns: (1) name; (2) morphological type (Lyon/Meudon Extragalactic Data base); (3) and (4) maximum rotational velocity and error; (5) innermost radius at which the H II velocity distribution overlaps the H I rotation; (6) first occurrence of a change in slope of the H II mean velocity curve.

at the line of nodes (assuming the H II is dynamically cold and in circular rotation). Table 2 lists for each galaxy the innermost radius at which the H II velocity distribution clearly overlaps the H I rotation curve, $R_{overlap}$ (in units of I-band scalelengths). The galaxies are transparent at radii larger than $R_{overlap}$, at least along the measured slit. This is consistent with earlier claims based on kinematic data that intermediate to late-type spiral galaxies are transparent in the outer parts (Bosma et al. 1992; Bosma 1995).

A second constraint on this 'transparency radius' is the first occurrence of a change in slope of the H II velocity curve, R_{slope} (Table 2). Outside the radius at which the slope first declines, the disc may be considered transparent (Bosma et al. 1992). The first clear change in slope of the H II velocity curves is listed in Table 2. These radii seem to indicate that the sample galaxies are sufficiently transparent at the heights where we have taken our spectra to study the kinematics in the optical except for the inner 0.5–1.0 I-band disc scalelengths. However, the simulations of H II rotation curves by Matthews & Wood (2001) suggest that this criterion does not hold at high optical depths. For galaxies which show a strong dust lane in the optical image the R_{slope} may therefore underestimate the true transparency radius.

The H II mean velocities and velocity dispersions are not easily corrected for the effect of line-of-sight projection. Still, in the inner parts the H II kinematics do contain additional information regarding the rotation curves. For galaxies in which the H II velocities connect smoothly to the rising part of the H I rotation curve, such as ESO 142-G24 and ESO 263-G15, the mean H II velocities probably trace the true rotation. In these cases the effects of dust extinction and projection are probably small. In many other cases, the H I data does not reveal the inner rising part of the rotation curve and the H II velocity distributions match the H I rotation curve on the outer flat part. Examples include ESO 201-G22, ESO 240-G11, ESO 446-G18 and ESO 564-G27. For these galaxies the H II mean velocities *plus* the 1σ velocity dispersions provide a firm lower limit to the true rotation. In the remaining cases, the H II is located far below the H I rotation curve in the inner parts and does not provide additional information. Examples are ESO 435-G25 and NGC 891. This behaviour is consistent with these galaxies having steeply rising rotation curves, for which the projection effect is expected to be most pronounced (Matthews & Wood 2001). Finally, although underrepresented in the current sample, in barred galaxies such as NGC 5529 the H II shows clear signs of non-circular motion in the inner parts. In that case the inner rotation curve cannot be determined.

The full rotation curves (Fig. 6, solid lines) were estimated by averaging the H I rotational velocities on both sides and taking in the inner parts, in those cases where the H II provides extra information, the maximum velocities reached by the H II. For the H I the rotational velocities obtained with the XV fitting method (Section 3.3) were used, or, in cases of poor signal-to-noise ratio the envelope-tracing results (Paper II). For the H II, the sum of the H II mean velocity and the velocity dispersion was adopted. Although this sum may not reach the true circular velocity of the H II (Matthews & Wood 2001), it approximates this circular velocity far better than simply taking the mean velocity curve. The symmetric rotation curves shown in Fig. 6 are a cubic spline interpolation of the combined points and the origin.

Most of the rotation curves are asymptotically flat. In addition, there are two examples of rotation curves that are slowly rising up to the last measured point, ESO 269-G15 and ESO 435-G50. For ESO 240-G11, ESO 435-G14 and ESO 564-G27 the rotation curve shows a small decline in the outer parts. In two other spirals, ESO 240-G11 and NGC 891, the adopted rotation curve has an inner maximum, although ESO 435-G25 and NGC 5529, for which no H I or H II information is available in the inner parts, may have similar maxima. The maxima of the adopted rotation curves are given in Table 2, where for ESO 240-G11 not the inner maximum but the secondary maximum is listed. The rotation curves will be used in conjunction with the observed stellar kinematics to construct dynamical models of the stellar discs (Paper IV).

In many of the XV diagrams the H II mainly coincides with the high-density H I. In the outer parts, the H II mean velocities are often aligned with a bright H I 'ridge' and form a slightly curved structure, which points roughly at the dynamical centre. This co-location of H I and H II further strengthens the case for transparency at these radii. Clear examples are ESO 142-G24, ESO 263-G15, ESO 435-G25, ESO 564-G27, NGC 5529 and NGC 891. These curved structures are highly suggestive of well-developed spiral arms. A concentration of H II regions in spiral arms would also, at least partly, explain the significantly smaller velocity broadening in H II compared with H I. This effect, first reported by Bosma (1995), is also expected if the H II regions do not extend as far out in galactocentric radius as the H I. Indeed, in those galaxies for which the slit covers the entire radial range over which H I is detected, there is a lack of H II regions at large projected radii and in the H I velocity tails towards the systemic velocity. Conspicuous examples are ESO 240-G11, ESO 263-G15, ESO 435-G15 and ESO 564-G27. It is, however, important to note that effects resulting from the optical slit being much narrower than the vertical extent of the H I and from a possible residual inclination of these systems has to be taken into account. Given that the ridge structures often seem to occur in the outer parts where the rotation curve is approximately flat, the exact location of the H II mean velocities may actually be used to reconstruct the spiral arm shapes. This could put the morphological classification of edge-on spirals, which is currently based purely on bulge to disc ratios, on a firmer footing. A final notable effect which is present in some cases is a systematic asymmetry between the H II velocities on either side of the galaxy. Examples are ESO 435-G14 and ESO 435-G50. This may perhaps be caused by the edge-on view of spiral

arms if the dust is situated on the inner edges of the arms, such that on the receding side it may obscure the H II regions.

6 CONCLUSIONS

We have pointed out that the envelope-tracing method for deriving the rotation curves of edge-on spiral galaxies is reliable only in the outer, flat parts of the rotation curve. At small radii the effects of beam-smearing and the projection have to be taken into account. A new technique is presented for determining the rotation curves of edge-on spiral galaxies. The major axis XV diagram of the gas is deprojected under the assumptions of pure circular motion, transparency and axisymmetry. This deprojection is performed via a least-squares fit of a set of concentric, coplanar rings according to an outside–in ('onion peel') approach. The advantage of this XV fitting method is that it naturally corrects for the line-of-sight projection and beam smearing. This allows an investigation of the gas kinematics in the inner regions which are shielded by emission from large galactocentric radii seen in projection. Monte Carlo simulations of the method illustrate its viability and provide errors.

The XV fitting method is applied to good quality H I XV diagrams of eight edge-on spirals. These galaxies show only moderate warping, are transparent in the H I line (except NGC 891) and show no evidence for strong non-circular motions. For ESO 142-G24 and ESO 263-G15 the XV fitting method reveals the rising part of the rotation curve. For the other galaxies the XV fits either show a deficiency of H I at small galactocentric radii or are limited by beam smearing in the innermost parts. A rule of thumb is that the peak signal to the root-mean-squared noise level in the XV diagram needs to be at least 15 in order for the XV fitting technique to improve upon the envelope-tracing method.

A comparison of the H I rotation curves with the H II kinematics for 16 edge-on spirals confirms that intermediate- to late-type spiral galaxies are transparent in the outer parts. In particular, the H II velocity distribution (mean velocity *plus* velocity dispersion) already matches the H I rotation within 1–2 *I*-band disc scalelengths, providing strong evidence for transparency at larger radii. Although not as robust, the first occurrence of a change in slope of the H II velocity curve indicates that the galaxies in the present sample are transparent except for the inner 0.5–1.0 disc scalelengths. Estimates of the full rotation curves are obtained by combining the information from the H I and H II kinematics. The resulting rotation curves have shapes similar to those of less-inclined spirals, including slowly rising rotation curves, declining rotation curves, and rotation curves with a steep inner rise and inner maximum. In the XV diagram, the H II is mainly found in regions of high-density H I, often forming curved 'ridges'. In addition, the velocity broadening of the H II is less than that of the H I. Both of these properties can be explained if the H II is mainly confined to spiral arms and does not extend out to the edge of the H I layer.

ACKNOWLEDGMENTS

We would like to thank Erwin de Blok, Iñigo García-Ruiz and Renzo Sancisi for valuable comments, criticism and suggestions. Rob Swaters kindly provided the H I data of NGC 891.

REFERENCES

Alton P.B., Xilouris E.M., Bianchi S., Davies J.I., Kylafis N.D., 2000, A&A, 356, 795
Aronica G., Athanassoula E., Bureau M., Bosma A., Dettmar R.-J., Vergani D., Pohlen M., 2003, ApS&S, 284, 753
Begeman K.G., 1987, PhD thesis, Univ. Groningen
Bosma A., 1991, in Casertano S., Sackett P.D., Briggs F.H., eds, Warped Discs and Inclined Rings Around Galaxies, Cambridge Univ. Press, Cambridge, p. 181
Bosma A., 1995, in Davies J.I., Burstein D., eds, Vol. 469, Proc. NATO Advanced Study Institute (ASI) Series C, The Opacity of Spiral Discs. Kluwer Academic Publishers, Dordrecht, p. 317
Bosma A., Byun Y., Freeman K.C., Athanassoula E., 1992, ApJ, 400, 21
Bottema R., 1996, A&A, 306, 345
Bottema R., Shostak G.S., van der Kruit P.C., 1987, Nat, 328, 401
Briggs F.H., 1990, ApJ, 352, 15
Bureau M., Freeman K.C., 1999, AJ, 118, 126
Christodoulou D.M., Tohline J.E., Steiman-Cameron T.Y., 1993, ApJ, 416, 74
Collins J.A., Rand R.J., Duric N., Walterbos R.A.M., 2000, ApJ, 536, 645
Dalcanton J.J., Bernstein R.A., 2002, AJ, 124, 1328
de Blok W.J.G., McGaugh S.S., Bosma A., Rubin V.C., 2001, ApJ, 552, 23
de Grijs R., 1997, PhD thesis, Univ. Groningen (http://www.ub.rug.nl/eldoc/dis/science/r.de.grijs)
de Grijs R., 1998, MNRAS, 299, 595
de Grijs R., Peletier R.F., van der Kruit P.C., 1997, A&A, 327, 966
Dickey J.M., Brinks E., 1993, ApJ, 405, 153
Fraternali F., van Moorsel G., Sancisi R., Oosterloo T., 2002, AJ, 123, 3124
García-Ruiz I., Sancisi R., Kuijken K., 2002, A&A, 394, 769
Goad J.W., Roberts M.S., 1981, ApJ, 250, 79
Howk J.C., Savage B.D., 1999, AJ, 117, 2077
Irwin J.A., 1994, ApJ, 429, 618
Kent S.M., 1986, AJ, 91, 1301
Kregel M., 2003, PhD thesis, Univ. Groningen (http://www.ub.rug.nl/eldoc/dis/science/m.kregel)
Kregel M., van der Kruit P.C., 2004, MNRAS, submitted (Paper IV)
Kregel M., van der Kruit P.C., de Grijs R., 2002, MNRAS, 334, 646
Kregel M., van der Kruit P.C., Freeman K.C., 2004a, MNRAS, in press (Paper I; doi:10.1111/j.1365-2966.2004.07864.x)
Kregel M., van der Kruit P.C., de Blok W.J.G., 2004b, MNRAS, in press (Paper II; doi:10.1111/j.1365-2966.2004.07990.x)
Kregel M., van der Kruit P.C., Freeman K.C., 2004c, MNRAS, sumitted (Paper V)
Kuchinski L.E., Terndrup D.M., Gordon K.D., Witt A.N., 1998, AJ, 115, 1438
Kuijken K., Merrifield M.R., 1995, ApJ, 443, L13
Makarov D.I., Karachentsev I.D., Burennkov A.N., Tyurina N.V., Korotkova G.G., 1997, Astron. Lett., 23, 638
Matthews L.D., Wood K., 2001, ApJ, 548, 150
Nelder J.A., Mead R., 1965, Comput. J., 7, 308
Olling R.P., 1996, AJ, 112, 457
Palunas P., Williams T.B., 2000, AJ, 120, 2884
Persic M., Salucci P., 1995, ApJS, 99, 501
Press W.H., Teukolsky S.A., Vetterling W.T., Flannery B.P., 1992, Numerical Recipes, 2nd edn, Cambridge Univ. Press, New York
Rand R.J., 1994, A&A, 285, 833
Rupen M.P., 1991, AJ, 102, 48
Sackett P.D., Morrison H.L., Harding P., Boroson T.A., 1994, Nat, 370, 441
Sancisi R., 1976, A&A, 53, 159
Sancisi R., Allen R., 1979, A&A, 74, 73
Sofue Y., 1996, ApJ, 458, 120
Sofue Y., Koda J., Nakanishi H., Onodera S., 2003, PASJ, 55, 59
Swaters R.A., 1999, PhD thesis, Univ. Groningen (http://www.ub.rug.nl/eldoc/dis/science/r.a.swaters)
Swaters R.A., Sancisi R., van der Hulst J.M., 1997, ApJ, 491, 140
Swaters R.A., Madore B.F., van den Bosch F.C., Balcells M., 2003, ApJ, 583, 732
van der Kruit P.C., 1981, A&A, 99, 298
van der Kruit P.C., Searle L., 1981a, A&A, 95, 105, (KS1)
van der Kruit P.C., Searle L., 1981b, A&A, 95, 116, (KS2)
van der Kruit P.C., Searle L., 1982, A&A, 110, 61, (KS3)
van der Marel R.P., Franx M., 1993, ApJ, 407, 525

Verheijen M.A.W., 1997, PhD thesis, Univ. Groningen (http://www.ub.rug.nl/eldoc/dis/science/m.a.w.verheijen)
Warmels R.H., 1988, A&AS, 72, 427

APPENDIX A: COMPLEX INNER GAS KINEMATICS

Fig. A1 displays close-ups of the XV diagrams of ESO 240-G11 and NGC 5529. These two galaxies show, both in the neutral and the ionized gas, an additional inner component which rises steeply in velocity. Together with the normal slowly rising component, this gives the H II in the XV diagram an 'X' shaped appearance. This signature suggests that both of these galaxies contain an inner bar (Kuijken & Merrifield 1995; Bureau & Freeman 1999). In the top panel of Fig. A1 the Hβ mean velocities at the FORS2 slit position (2 arcsec away from the major axis) are also shown (triangles). These velocities are asymmetric with respect to the galaxy centre, an asymmetry that is also present in the stellar velocities (see Paper IV).

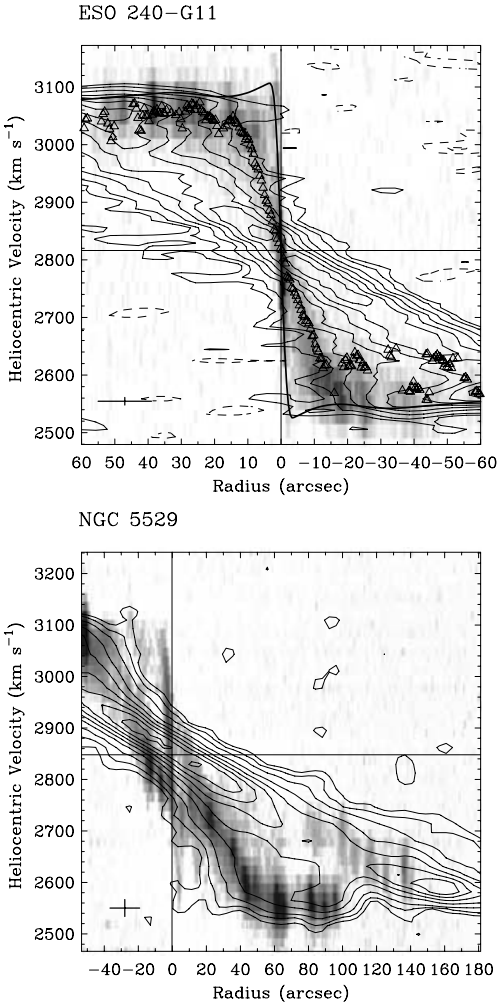

Figure A1. Close-ups of the XV diagrams that show complex gas kinematics in the central region. Top, ESO 240-G11, the [N II] line (grey-scale) overlayed on the H I XV diagram (contours). Contour levels are as in Fig. 5. The triangles indicate the Hβ mean velocities obtained from the VLT-FORS2 spectrum and the solid line shows the adopted rotation curve. Bottom, NGC 5529, the Hα line (grey-scale) overlayed on the H I XV diagram (contours). Contour levels are as in Fig. 6. In both panels the velocities use the radio definition.

This paper has been typeset from a TEX/LATEX file prepared by the author.